EES Catalysis

PAPER

View Article Online
View Journal | View Issue

Cite this: *EES Catal.*, 2026, 4, 213

Core–shell structured PtCu/C applied in a high-temperature direct ethanol electroreformer to produce green H_2 at reduced energy demand with high CO_2 selectivity: performance and techno-economic analyses

Dryade F. de Paula,†[a] Rudy Crisafulli,†[a] Jesús González-Cobos,[b] Ángel Caravaca‡[b] and José J. Linares *[a]

Three different electrocatalysts have been prepared, characterized, and applied to a high-temperature direct ethanol polymer electrolyte membrane electroreformer (DEPEME) based on the removal of surface Cu from the initial Pt_xCu/C (x = 3, 1, and 1/3) raw materials. The resulting structure consisted of a Pt-enriched shell on a PtCu alloy core deposited on C [alloyed $Pt_xCu@Pt_yCu/C$ ($y \gg x$)], achieved after the acid treatment of the prepared catalysts, in a core–shell (CS) configuration. This structure is confirmed by X-ray diffraction, which evidences the formation of a PtCu alloy, whereas X-ray photoelectron spectroscopy reveals an enriched Pt shell. Finally, transmission electron microscopy images revealed the dispersed deposition of metal nanoparticles at the nanoscale range. Regarding the electrochemical performance, the CS materials displayed enhanced CO tolerance and ethanol electro-oxidation (EEO) performance, characterized by increased current density and a lower onset potential compared to Pt/C. These results were corroborated at the high-temperature DEPEME condition of 150 °C. Moreover, the monitoring of the EEO products revealed that the CS PtCu materials notably enhanced the selectivity for CO_2, resulting in a desirable combination of high hydrogen production rate (0.205 kg of H_2 m^{-2} h^{-1}) and CO_2 selectivity (close to 50%) at a reduced energy consumption (25.46 kWh kg H_2^{-1}). Finally, a techno-economic analysis presents the potential of using ethanol produced in a sugarcane plant from bagasse (second-generation) and estimates the cost of H_2 produced compared to that of a PEM water electrolyzer.

Received 9th July 2025,
Accepted 16th October 2025

DOI: 10.1039/d5ey00210a

rsc.li/eescatalysis

Broader context

Classical green H_2 is produced by water electrolysis, which is punished with high total costs, initial investment, and operating costs. Ethanol-based electroreforming emerges as an alternative due to its renewable origin and lower energy demand. However, classical Direct Ethanol PEM electroreformers (DEPEME) exhibit low H_2 yield (below 33.3%) due to the incomplete oxidation of ethanol. We propose an advanced electrocatalyst architecture, based on a Pt-enriched Pt_yCu/C core on an alloyed Pt_xCu shell ($y \gg x$), applied to a high-temperature DEPEME, aiming to promote activity and H_2 yield due to high CO_2 selectivity. The electrocatalyst obtained from the acid treatment of the base $PtCu_3/C$ can produce H_2 at a higher rate with a higher yield (50%), and a lower energy consumption per kg of H_2 compared to Pt/C. Furthermore, the energy requirement of the DEPEME is half that of water electrolysis (PEME). Under this scenario, a technoeconomic analysis has been conducted under various hypotheses, including the specific price of the electrolyzer/electroreformer, electricity prices, DEPEME operating conditions, and expected lifetime, revealing the conditions under which DEPEME or PEME is the most appropriate option. The results reveal that DEPEME might indeed be an interesting alternative for producing green H_2 at competitive costs.

[a] *Chemical Process Development Laboratory, University of Brasilia, Campus Universitário Darcy Ribeiro, 70910-900 Brasília, Distrito Federal, Brazil. E-mail: joselinares@unb.br*

[b] *Université Claude Bernard Lyon 1, CNRS, UMR 5256, IRCELYON, 2 avenue Albert Einstein, Villeurbanne F-69622, France*

† Current address: Nuclear and Energy Research Institute (IPEN), Avenida Prof. Lineu Prestes, 2242, 05508-000 São Paulo, Brazil.

‡ Current address: Department of Mechanical, Chemical and Industrial Design Engineering, Universidad Politécnica de Madrid, Escuela Técnica Superior de Ingeniería y Diseño Industrial, Ronda de Valencia 3, 28012, Madrid, Spain.

1. Introduction

In later years, hydrogen gained more relevance due to its crucial role as an energy vector and as a key chemical in fertilizers, oil, petrochemicals, metallurgy, electronics, and the food industry.[1] This scenario is further supported by the policies worldwide that have been implemented to accelerate the transition from fossil to renewable sources, in which hydrogen serves as an energy carrier to match energy supply and demand.[2,3] Previsions made by the International Energy Agency (IEA) have foreseen an increase of 50% in 2030 compared to the most recent production of 97 Mt of H_2 in 2023 (China as the first producer, followed by the USA), with a primary participation of hydrogen coming from electrolysis fed by renewable sources (green hydrogen). Notwithstanding, the current hydrogen production is mainly based on fossil fuels, especially from natural gas steam reforming and coal gasification.[4] Low-carbon emission hydrogen is scarce, accounting for only 0.7% of the global production, primarily derived from fossil fuels with carbon capture systems. Green hydrogen, produced from water electrolysis fed with renewable sources, has a minuscule participation of 0.1%.

The main shortcomings of green H_2 development stem from high capital expenditures (CAPEX) and electricity costs, which are introduced into operational expenditures (OPEX). High OPEXs are related to the high energy consumption from the necessary high cell voltage, 1.6–1.8 V, resulting in a demand of over 55 kWh per kg of H_2.[5] Such high voltage comes from the high overvoltage of the oxygen evolution reaction (OER, >1.23 V *vs.* standard hydrogen electrode, SHE). Therefore, replacing the OER with other less energy-demanding reactions, such as the oxidation of biomass-based organic compounds, including alcohols, sugars, lignin, and derivatives[6–8] (theoretical values *circa* 0.0 V *vs.* SHE), can be an alternative. Furthermore, recent studies demonstrate that this principle can also be combined with wastewater treatment.[9–11] This approach could achieve energy savings above 40%, with values well below 30 kWh per kg of H_2.[6]

Ethanol is a promising candidate for electroreforming, given its renewable origin from edible biomass (sugarcane, corn, beetroot, producing the first-generation ethanol).[12] Second-generation ethanol would be more interesting, coming from wastes (lignocellulosic materials such as bagasse and other residues of sugarcane processing with no commercial value),[13,14] thereby avoiding potential conflicts with food stocks. Ethanol electrorefoming has been successfully applied to alkaline electrolyzers,[15,16] alkaline exchange membrane electrolyzers,[17,18] or polymer electrolyte membrane electrolyzers.[19–23] All these electroreformers produced hydrogen at a lower energy cost than water electrolysis at low reaction temperatures. Nevertheless, these systems present some historical limitations associated with the slow kinetics of ethanol electro-oxidation (EEO) and incomplete ethanol oxidation, as acetaldehyde and acetic acid are the primary products of EEO.[24–26] One alternative to overcome this limitation is to increase the temperature to 150–175 °C to improve the EEO kinetics. Moreover, the CO_2 selectivity can be elevated up to 55% if temperatures between 150 and 175 °C are used, as demonstrated elsewhere.[27,28] For this purpose, it is necessary to use H_3PO_4-doped polybenzimidazole (PBI) membranes, given their capacity to transport protons at those high temperatures with excellent mechanical, thermal, and chemical stability.[29] Furthermore, their low ethanol permeability allows them to operate with ethanol concentrations as high as 5.7 mol L^{-1} (perfluorosulfonated electrolyzers typically operate with 1 mol L^{-1} ethanol due to ethanol crossover[30]), resulting in a larger potential for hydrogen production per liter of fuel. Notably, the proposed temperature range of 150–175 °C is still lower than that of the electrolyzers classically denoted as high-temperature electrolyzers, specifically the solid oxide electrolysis cells (SOEC), which operate between 750 and 850 °C. Thus, common operational and maintenance shortcomings of SOEC are avoided, *e.g.*, increased heating energy demands, limited lifetime of cell components, and hindered dynamic behavior with slow response time during start-up, shutdown, and adjustment of the electrolyzer.[31] The catalyst is also a key element in determining the EEO product distribution. Previous studies have shown that Pt is the best electrocatalyst for maximizing CO_2 selectivity and, thus, the specific hydrogen production compared to multimetallic materials in high-temperature direct ethanol polymer electrolyte membrane fuel cells (DEPEMFC), whose anode configuration is similar to that of a high-temperature direct ethanol PEM electroreformer (DEPEME).[28,32] Nevertheless, the electrochemical performance of Pt/C is lower than that of bimetallic materials (*e.g.*, PtRu and PtSn), so the practical hydrogen flow rate would be limited. Thereby, larger electrolyzers would be required to meet a specific H_2 demand. These results lead to a paradox: the performance *versus* the hydrogen produced compared to the potential one.

Bimetallic materials are known to improve their performance by two mechanisms: (i) bifunctional, in which adjacent liable metal atoms supply oxygenated species to the poisoned Pt sites to oxidize and release the ethanolic adsorbates formed during the EEO; (ii) electronic, in which the second metal alter the electronic states of Pt, modifying the adsorption strength of the species formed during the EEO. Generally, both mechanisms are present in bimetallic materials: part of the liable metal is alloyed with Pt (strong electronic effect), and the rest is in the form of oxide/s (powerful bifunctional effect), noting that both effects can be present in the alloy and the oxide/s.[33] Our experience showed that bimetallic materials preferentially form acetaldehyde (the most abundant) and acetic acid.[28,32]

A potential approach to overcoming the challenges mentioned above involves utilising a core–shell (CS) architecture, featuring a platinum-enriched shell surrounding an alloyed platinum core. The internal alloyed structure can maintain the electronic effect, while the Pt-enriched surface can stimulate the C–C scission. In this sense, a recent review has highlighted that this approach for facilitating the C–C cleavage in the EEO is attributed to electronic, lattice strain, and surface defect effects.[26] To prepare CS structures, the acid treatment of

an alloyed PtCu is considered to be a ref. 34, with successful results on EEO: Ammam and Bradley Easton[35] evidenced that a Pt-enriched surface of a PtCu alloy increased the EEO activity in terms of lower onset potential and higher current density, as well as improved stability to operating in potentiostatic and potentiodynamic conditions. Huang *et al.*[36] prepared a dealloyed PtCu material with a 70 mV lower onset potential than Pt/C, and a maximum current density that was 3.9 and 4.8 times higher in terms of active area and Pt mass, respectively. Furthermore, the authors observed a more extensive conversion of ethanol to CO_2. Finally, Castagna *et al.*[37] prepared dealloyed PtCu electrocatalysts with different Pt : Cu proportions, observing that the onset potential of the PtCu/C materials is downward shifted by 200 mV compared to the standard PtRu/C and that the maximum current density is 2.5–3 times higher for PtCu/C than for PtRu/C.

Such encouraging results have served as a basis for this work, in which CS PtCu/C (alloyed Pt_xCu@ enriched Pt_yCu ($y \gg x$)/C) nanoparticles with different Pt : Cu atomic ratios have been developed to be used in a direct ethanol polymer electrolyte membrane electroreformer at high temperature (150 °C). The base bimetallic materials were first synthesized using $NaBH_4$, then thermally treated in a reducing H_2 environment to promote the alloying of Pt and Cu, and finally, acid-treated to remove the labile Cu, resulting in the CS electrocatalysts. The prepared materials were physicochemically characterized by inductively coupled plasma optical emission spectroscopy (ICP-OES), X-ray diffraction (XRD), X-ray photoelectron spectroscopy (XPS), and transmission electron microscopy (TEM). The physicochemical parameters derived from these analyses facilitate an understanding of the electrochemical results obtained from cyclic voltammetry, CO stripping, EEO voltammetric curves, chronoamperometry, and ultimately, the results in the high-temperature DEPEME. Product distribution in the DEPEME has also been quantified by mass spectrometry (MS). Finally, a preliminary economic analysis is conducted to estimate the cost of hydrogen produced by this approach, which is proposed for the fertilization of a sugarcane farm coupled with an ethanol production plant, utilizing the potential ethanol that can be obtained from the bagasse waste.

2. Experimental

2.1. Synthesis of core–shell PtCu/C electrocatalysts

Electrocatalysts with an initial metal loading of 20 wt% on carbon black (Vulcan XC-72, Cabot Corp.) were prepared by chemical reduction with sodium borohydride. The metal precursors used were $CuCl_2{\cdot}2H_2O$ (Synth) in solid form and a solution of 5 g of $H_2PtCl_6{\cdot}6H_2O$ (Sigma Aldrich) in 100 mL of 2-propanol (Synth). To prepare 400 mg of catalyst, the required amount of $CuCl_2{\cdot}2H_2O$ was weighed and dissolved in approximately 190 mL of 2-propanol using a magnetic stirrer under a N_2 atmosphere. Once the $CuCl_2$ dissolved, 320 mg of carbon black and the required amount of Pt precursor were sequentially added to the 250 mL three-neck round-bottom flask. The three necks of the flask were covered to maintain the inert atmosphere, and the mixture was sonicated for 20 minutes to guarantee the dispersion of the carbon support and the metal precursors. The reduction solution was prepared in a 50 mL Erlenmeyer flask with a molar ratio of 5 mol of $NaBH_4$ (Vetec) for each metal gram atom in 20 mL of ultrapure water (Milli-Q, Millipore). This solution was added immediately to minimize borohydride hydrolysis. The reduction process was maintained for 2 h at 25 °C. In the first stage, the obtained powder was filtered, thoroughly washed with triple-distilled water, dried at 70 °C for 12 h, and then finely ground to produce the initial catalyst powder. With this procedure, Pt/C, Pt_xCu/C (nominal x = 3, 1, and 1/3), and Cu/C were synthesized. In the second stage, the five prepared materials were thermally treated in a H_2-reducing atmosphere (pure H_2) for 6 h at 170 °C at a pressure of 6 bar. In this sense, a recent TPR study of PtCu catalysts demonstrated the reducibility of both metal oxides (PtO_x and CuO_x) at temperatures between 150 and 250 °C in a 5 vol% H_2/He atmosphere.[38] Given that the applied temperature of the thermal treatment was in the lower range of the cited work, a higher H_2 pressure was applied to this study to stimulate the alloying of Pt and Cu further. A constant flow of 5 mL min^{-1} was applied to promote the removal of the gases formed during the reduction of the oxides in the samples. This procedure produced the so-called base materials.

Once this process was completed, the bimetallic samples were acid-treated, with the expectation of removing the non-alloyed (labile) copper and the surface and subsurface copper atoms in the alloyed nanoparticles. The materials were treated with 9 mol L^{-1} concentrated HNO_3 (Vetec) for 1 h at room temperature. Next, the samples were repeatedly centrifuged (Centribio 80-2B Digital centrifuge) for 5 minutes at 4000 rpm until the supernatant was neutral. The samples were again dried in an oven for 12 h at 70 °C and ground to obtain the final CS PtCu/C materials (denoted with the same nominal Pt and Cu atomic ratios as in the base materials).

2.2. Physicochemical characterization of the electrocatalysts

The metallic percentages of the samples were estimated by thermogravimetry in a Shimadzu DTG-60H thermal analyzer (Shimadzu) in an air atmosphere. The samples were heated from room temperature to 900 °C at 10 °C min^{-1}. In the 500–700 °C range, an abrupt mass loss is associated with the carbon combustion, so the remaining mass is attributed to the metals. The Pt : Cu ratio was measured by ICP-OES (Ultima Expert Spectrometer, Horiba Scientific). The samples were digested in Teflon tubes with 1 mL of HNO_3 (65 wt/wt%, Sigma-Aldrich) and 3 mL of HCl (37 wt/wt%, Sigma-Aldrich). The tubes were closed and placed in an oven at 150 °C for metal digestion. Next, the reaction mixture was centrifuged to separate the supernatant, which was then used to determine the Pt : Cu atomic ratio.

To determine the crystallinity, average crystallite size, and alloy degree, XRD was carried out in a Rigaku Miniflex 300 diffractometer from 2θ angles between 20 and 90°, scan rate of 0.5° min^{-1}, step 0.05°. The applied radiation corresponded to

the Cu K_α (λ = 0,15046 nm). The average crystallite (d) size was obtained by the application of Scherrer's eqn (1), where K is a particle-shape-dependent constant (0.9 for spherical particles), λ is the wavelength of the incident radiation (1.5406 Å for Cu K_α), θ is the angle of the (hkl) peak, and $\beta_{(2\theta)}$ is the width in radians of the diffraction peak at half height.

$$d = \frac{k\lambda}{\beta_{(2\theta)} \cos\theta} \quad (1)$$

By applying Vegard's law (eqn (2)) to the PtCu bimetallic system, it is possible to estimate the alloying degree of the bimetallic material, where a_{PtCu} represents the lattice parameter of the bimetallic electrocatalyst, a_{Pt} the lattice parameter of Pt (0.3912 nm), a_{Cu} the lattice parameter of Cu (0.3601 nm), and x_{Cu} the Cu fraction in the PtCu alloy.

$$a_{PtCu} = x_{Cu}a_{Cu} + (1 - x_{Cu}) \quad (2)$$

eqn (3) calculates the percentage of Cu participating in the alloy ($Cu_{alloyed}$) to the total percentage of Cu, where Cu/Pt is the actual atomic ratio between the two metals (as estimated by ICP-OES).

$$Cu_{alloyed} = \frac{x_{Cu}}{(1 - x_{Cu})(Cu/Pt)} \quad (3)$$

XPS was performed using a Kratos Axis Ultra DLD, with Al K_α radiation (1486.6 eV) as the X-ray source, operating at 225 W, 15 kW, and 15 mA. A first survey spectrum was obtained between 0 and 1200 eV, with a step size of 1 eV and a residence time of 100 ms. Afterward, spectra in the regions of C 1s, O 1s, Cu $2p_{3/2,1/2}$, and Pt $4f_{7/2,5/2}$ were recorded with a step of 0.1 V and a residence time of 200 ms. The charge effect neutralization of the samples was performed by emitting a low-energy beam. The spectra were calibrated using the binding energy of graphite, C 1s band (C–C and C–H bonds). The mathematical treatment of the data was carried out after subtracting the Shirley-type background correction.[39]

TEM images were obtained in a JEOL 2100 microscope operated at 200 kV with a point-to-point resolution of 0.19 Å. Particle size distributions were obtained from 300 particles. The average particle size (d_{TEM}) was estimated by eqn (4), where d_i is the size of the considered particles in the size range i, and n_i is the number of particles with that size.

$$d_{TEM} = \frac{\sum_i n_i d_i}{\sum_i n_i} \quad (4)$$

Line mapping profiles were obtained using a FEI Tecnai G^2 F20 at 200 kV, equipped with a scanning transmission electron microscope system (STEM) and an EDS detector, to understand the potential formation of core–shell structures better.

2.3. Electrochemical characterization and evaluation of EEO performance

Preliminary electrochemical measurements were carried out in a three-electrode glass cell at room temperature using the ultra-thin coating. A 4 cm^2 platinized Pt gaze was used as the auxiliary electrode, with an Ag/AgCl/3.5 mol L^{-1} KCl reference electrode. The working electrode (WE) was a circular reticulated vitreous carbon (5 mm ϕ), onto which 10 μL of ink formed by 4 mg of electrocatalyst, 10 μL of a Nafion emulsion (5 wt% in a mixture of aliphatic alcohols, IonPower) and 1 mL of isopropyl alcohol (Dinâmica), subsequently sonicated for 30 min, was deposited and let to dry. Electrochemical measurements were performed using a μ-Autolab (model Type III) potentiostat/galvanostat, coupled to a personal computer and general-purpose electrochemical system (GPES) software. Blank cyclic voltammetries (CV) were performed in 0.5 mol L^{-1} H_2SO_4 (Vetec) at a scan rate of 0.05 V s^{-1}. CO stripping was also carried out. The solution was initially deaerated with N_2 for 15 min, after which CO was bubbled for 20 min, maintaining the WE at 0.1 V *vs.* RHE. In the sequence, N_2 was bubbled for 40 minutes to remove the dissolved CO. Three consecutive scans were performed, with the first scan used for CO oxidation and the third as the baseline to calculate the active area and the CO onset potential. The electrochemically active surface area (EASA) can be estimated from the integration of the CO-oxidation peak (A_{CO}) by eqn (5), where ν is the scan rate (same as in the blank voltammetries) and Q_{CO} is the geometric charge associated with the CO electrodesorption on Pt (0.42 mC cm^{-2}).[40]

$$EASA = \frac{A_{CO}}{\nu Q_{CO}} \quad (5)$$

EEO was also analyzed by CV using a 5 mol L^{-1} ethanol and 1 mol L^{-1} phosphoric acid (Vetec) solution. This high ethanol concentration was intended to mimic the high concentrations typically used in electroreformers. In this case, the scan rate was reduced to 0.005 V s^{-1}. Finally, chronoamperometric curves were applied at 0.68 V *vs.* RHE for 2 h to assess the stability and poisoning tolerance of the electrocatalysts.

2.4. Assessment of high-temperature direct ethanol polymer electrolyte membrane electroreformer (DEPEME)

The DEPEME experiments were conducted at 150 °C with different anodes/cathodes prepared by paint-brushing (active area of 4 cm^2). A catalytic slurry was formed by mixing the required mass of catalytic powder to obtain an overall catalyst loading of 10 mg cm^{-2} (corresponding to a metal loading of 2 mg cm^{-2} Pt in the case of the Pt/C or lower for the CS materials due to the partial removal of Cu), an amount of Nafion corresponding to 10 wt% of the total catalyst loading, 0.2 mL of water, and 0.4 mL of isopropyl alcohol. This slurry was sonicated for 30 min and paint-brushed onto the Zoltek PX30 carbon cloth (Zoltek). The cathode was prepared following the same protocol. In this case, a commercial 20 wt% Pt/C (Premetek Inc., USA) was used as the electrocatalyst with a Pt loading of 0.5 mg cm^{-2}. Once the catalytic layer deposition was completed, the electrodes were dried for 1 h at 80 °C in an oven and impregnated with a 10 wt% H_3PO_4 (Vetec) solution (30 mg cm^{-2}). This impregnation provides proton conduction to the electrode and softens the electrode/membrane contact. A H_3PO_4-doped PBI membrane (PBI membrane Blue World

Technologies ApS, Denmark, soaked for 2 weeks in 85 wt% H_3PO_4) was sandwiched between the electrodes and hot-pressed for 15 minutes at 150 °C, applying a load of 1 ton. The membrane-electrode-assembly (MEA) was placed in a homemade graphite-built single-cell electrolyzer. Details about the experimental setup can be found elsewhere, including the protocol for using mass spectrometry to establish product selectivity.[27] It is important to note that the fuel used was a mixture of ethanol and water in the volumetric ratio 1 : 2 (corresponding to 5.7 mol L^{-1} ethanol) based on a previous optimization study.[41]

3. Results and discussion

3.1. Characterization of the electrocatalysts

Fig. 1 presents the overall metal percentages of the base and CS materials and the Pt : Cu ratio in the bimetallic samples. As can be seen, the actual overall metal percentages and Pt : Cu fraction of the base materials are close to the nominal ones. On the other hand, the CS materials exhibit a decrease in the Cu percentage, which is higher as the Cu percentage increases in the original material (Cu losses of 36% for Pt_3Cu/C, 44% for PtCu/C, and 80% for $PtCu_3$/C). The proposed acid treatment decreases the metal loading from the Cu lixiviation (Pt wt. percentages remain stable, Fig. 1a). Further, it increases the Pt : Cu atomic ratio, especially in the original $PtCu_3$/C case. These results represent the first evidence of copper removal through acid treatment. More relevant information related to the nature of this copper can be extracted from the XRD and XPS analyses.

Fig. 2 shows the base and CS catalysts' XRD diffractograms. All spectra show a diffraction peak at *ca.* 25°, attributed to Vulcan XC-72 support.[42–44] The Cu/C displays the peaks associated with metallic Cu and Cu_2O. In the case of the Pt/C, and base Pt_3Cu/C and PtCu/C, the peaks related to Pt crystalline facets are present, though shifted to higher angles due to the lattice contraction by PtCu alloying, as observed in previous studies on PtCu alloys.[45] Base $PtCu_3$/C shows peaks associated with two segregated crystals, PtCu alloy and CuO, with no apparent presence of other reduced Cu species. The acid treatment brings notable alterations to the CS $PtCu_3$/C, with the complete disappearance of the Cu diffraction peaks. Furthermore, a slight shift to lower angles can be observed for the three CS catalysts compared to the base ones, evidencing a decrease in the alloying degree. These results evince significant structural rearrangements caused by the acid treatment.

Table 1 presents the average crystallite sizes, lattice parameters, alloy composition, and the distribution of alloyed and non-alloyed Cu, providing relevant quantitative information. As can be seen, Pt/C possesses a larger average crystallite size compared to the bimetallic materials, which further diminishes as the Cu fraction increases. This behavior is attributed to the protective role exerted by Cu (or copper oxide) during the growth of the crystal embryos, leading to the observed smaller

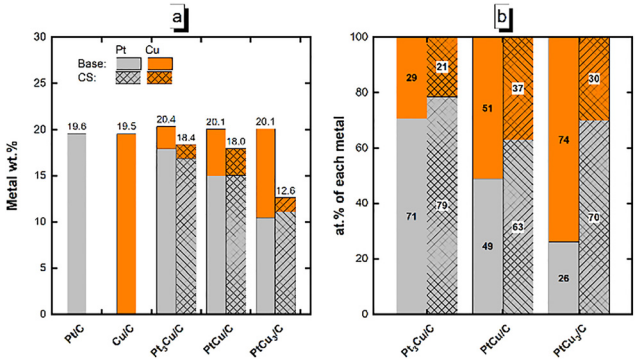

Fig. 1 (a) Overall metal percentages (labels include the total metallic wt%); and (b) distribution percentages of each metal (see labels) in the overall metallic charge of the different catalysts.

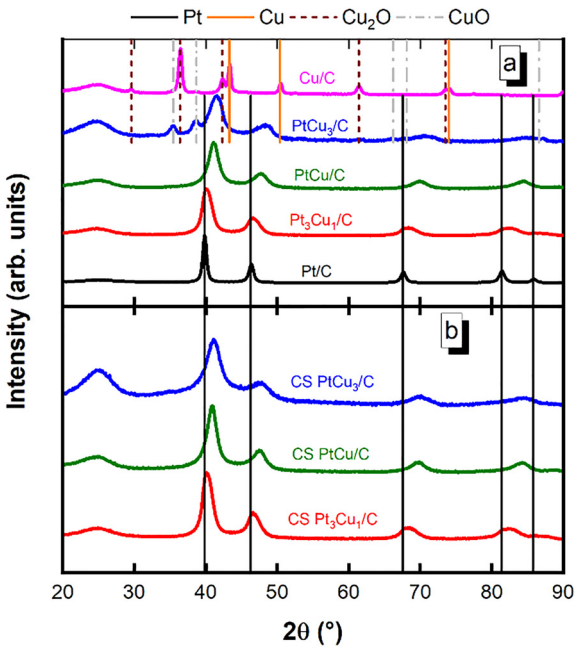

Fig. 2 Diffractograms of the prepared electrocatalysts: (a) base, and (b) CS (vertical lines and legends correspond to the XRD peaks of the different species present in the electrocatalysts).

PtCu crystals.[46,47] The CS materials possess smaller crystallite sizes due to the lixiviation effect exerted by the acid, reducing the size of the alloyed PtCu crystals. Regarding the lattice parameter and alloying degree, the acid treatment leads to an expansion in the lattice parameter and a decay in the Cu fraction in the alloy. The removal of part of the Cu inserted in the alloyed face-centered cubic (fcc) PtCu crystals may be responsible for the lattice dilation, confirming the structural changes induced by the acid treatment.

In the case of the percentage of Cu integrated in the alloy, the acid treatment increases this parameter primarily due to the removal of part of the segregated Cu during the acid treatment, especially in the case of the CS $PtCu_3$/C. Nevertheless, a fraction of non-alloyed Cu remains in the CS Pt_3Cu/

Table 1 Average crystallite sizes and lattice parameters of Pt/C and PtCu/C electrocatalysts obtained by XRD and average particle size obtained from TEM images (in the case of the Cu/C material, the three observed phases have also been estimated)

		Crystallite size (nm)		Lattice parameter (nm)		x value in the $Pt_{1-x}Cu_x$ alloy		% of alloyed Cu	
Material		Base	CS	Base	CS	Base	CS	Base	CS
Pt/C		7.0	—	0.3915	—	—	—	—	—
Pt_3Cu/C		5.6	5.3	0.3878	0.3883	0.12	0.11	34	45
PtCu/C		5.3	5.2	0.3805	0.3816	0.37	0.33	55	83
$PtCu_3$/C	$PtCu_3$	4.0	3.6	0.3775	0.3807	0.46	0.36	30	130[a]
	CuO	9.0	—	—	—	—	—	—	—
Cu/C	Cu	15.0	—	0.3613	—	—	—	—	—
	Cu_2O	11.6	—	0.4270	—	—	—	—	—

[a] More alloyed Cu than available; see discussion in the text.

C and PtCu/C. XRD patterns and later XPS results indicate that most of the remaining Cu is in a segregated, amorphous, reduced form (Cu(0) or Cu(I)), which appears to be more resistant to acid treatment. The CS $PtCu_3$/C shows a higher fraction of alloyed Cu than available. This behavior can be explained by the removal of Cu from the PtCu alloy without complete rearrangement of the crystallites (lattice expansion). Such evidence can be of interest, as it may be a source of nanoparticle structural defects, particularly relevant to the ethanol electro-oxidation.[48]

XPS analyses of the base and CS materials were conducted to obtain comprehensive compositional and oxidation state information, as well as to provide a clearer radiography of the bimetallic nanoparticles' surface (Pt 4f and Cu 2p spectra are presented in Fig. S1 and S2, respectively). The Cu surface percentages and their comparison with the total and alloyed Cu are presented in Fig. 3, with the corresponding percentages inserted in a table. This combined analysis helps elucidate the formation of Pt-enriched surfaces on alloyed PtCu nanoparticles. Additionally, it provides information about the nature of the removed Cu, whether segregated or, more interestingly, alloyed. Some remarks are listed below:

- The first observation is the significant enrichment of the CS nanoparticle surfaces in Pt due to the removal of the most exposed Cu (the Cu fraction in the surface becomes smaller than the overall Cu).
- The base electrocatalysts present a smaller percentage of Cu in the alloy than on the surface. Besides, the increase in total Cu favors the existence of a large fraction of segregated copper and/or PtCu alloyed nanoparticles with a Cu-enriched surface.
- In the case of CS materials, the alloyed Cu is higher than that on the surface, supporting the formation of a Pt-enriched core in the PtCu alloyed nanoparticles.
- Finally, the higher percentage of Cu in bulk compared to the alloy in the CS Pt_3Cu/C and PtCu/C (not for CS $PtCu_3$/C) evidences the presence of a small fraction of non-alloyed copper.

As shown in Fig. S1, all the Pt materials exhibit Pt(0) asymmetric doublets at binding energies (BEs) of 71.5 and 74.8 eV, with a growing contribution from the Cu 3p peak as the Cu fraction increases, particularly in the case of the base materials.[49] As expected, this latter contribution diminishes

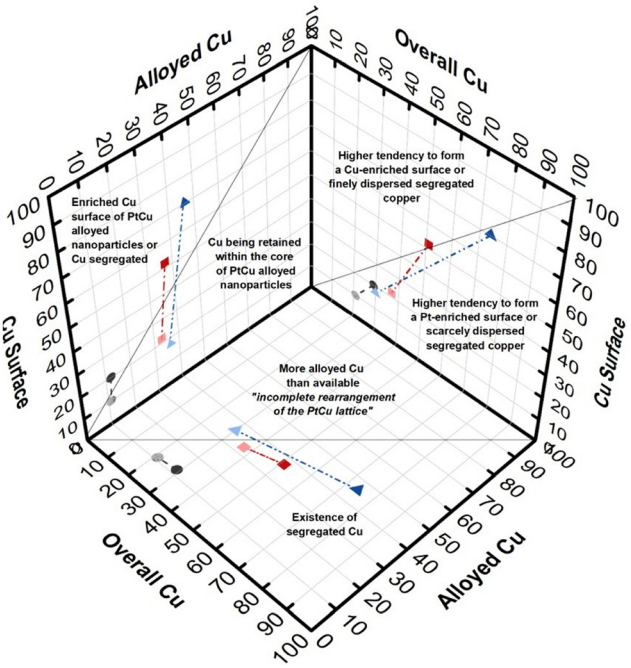

Pt:Cu percentages						
Material	Base			CS		
	Overall	Alloy	Surface	Overall	Alloy	Surface
Pt_3Cu/C	71:29	88:12	80:20	79:21	89:11	90:10
PtCu/C	49:51	63:37	48:52	63:37	67:33	78:22
$PtCu_3$/C	26:74	54:46	30:70	70:30	64:36	83:17

Fig. 3 Projections of the Cu atomic percentages on the surface (XPS), in the PtCu alloy (XRD), and the overall (ICP-OES) (●●: Pt_3Cu/C; ■■: PtCu/C; ▲▲: $PtCu_3$/C; light symbols correspond to CS materials). The inset table collects the corresponding percentages for each analysis.

after the acid treatment due to the removal of surface copper. One interesting observation is that in the base materials and the CS Pt_3Cu/C and CS PtCu/C, the Pt 4f BE remains constant regardless of the formation of the PtCu alloy, which is somewhat unexpected. In literature, down- and upshifts in the BE have been reported depending on the dominant mechanism of the electron transfer between Pt and Cu: (a) a BE decrease due to the higher electronegativity of Pt compared to Cu, resulting in an electron transfer from the latter to the former;[50–53] (b) a BE increase,[45,54–57] attributed to quantum confinement effects, coming from the differences in the work functions between Pt

and Pt alloys, as well as the rehybridization of d- and sp-bands after the alloy formation.[54,58,59] Lee *et al.*[60] reported scarce alterations in the Pt 4f BE for a PtCu bulk alloy. The authors attributed this result to the occupation of the Pt $d_{5/2}$ states, compensated by the deoccupation of the Pt $d_{3/2}$ electrons, leading to an almost null shift in the Pt 4f core-level binding energy. This electronic rearrangement may occur in our system, perhaps stimulated by the thermal treatment, leading to the invariant Pt 4f BE. In the case of the CS $PtCu_3$/C, there is a small upshift of the binding energy of 0.1 eV. Such a change may be attributed to the particular lattice strain generated in this material due to the insufficient rearrangement after the acid treatment with a compressed crystalline lattice.[56] This upshift alters the electronic environment by downshifting the Pt-d band center, reducing the eventual adsorption strength of the species involved in the electrochemical reaction.[56,58] Such electronic effects kinetically and mechanistically impact the EEO reaction.

In the case of the Cu 2p spectra (Fig. S2), all the materials, except the CS Pt_3Cu/C (absence of Cu(II)), present a combination of Cu (0 or I) and Cu(II) in different proportions. The values are collected in Table S1. The percentage of surface Cu(II) in the base materials increases with the total Cu content in the electrocatalyst. This result can be attributed to a larger fraction of segregated Cu being exposed to surface oxidation. The acid treatment results in CS materials in which Cu becomes minor on the surface of the nanoparticles. Moreover, the fraction of CuO is drastically reduced (or disappears), with most of the Cu in the form of metallic Cu or Cu_2O. Thus, the acid treatment seems to have preferentially attacked the Cu(II) form, enriching the nanoparticles' surface in reduced Cu(0 or I).

Fig. 4a–h shows the TEM images of the different electrocatalysts, including high-resolution images of the CS PtCu/C and CS $PtCu_3$/C (Fig. 4i and j), as well as the Boxplot of the particle size distribution (Fig. 4k) to obtain the most relevant statistical parameters (histograms of particle size distributions of the Pt-containing materials are presented in Fig. S3). As observed, the Pt/C presents relatively large nanoparticles (average diameter of 7.14 nm) and a wide size distribution, resulting from the use of the potent reducing agent $NaBH_4$ along with thermal treatment.[61] When Cu is added to Pt, we can observe a general tendency of mean particle size decay (down to 3.75 nm for $PtCu_3$/C), which is in qualitative agreement with the crystallite size results. In broad terms, the acid treatment results in a more heterogeneous particle size distribution, which can be attributed to particle size rearrangement or dissolution and redeposition caused by the corrosive action of nitric acid. The high-resolution TEM images of the CS PtCu/C and $PtCu_3$/C evidence the formation of rough, irregular (spongy-like) nanoparticle surfaces due to the removal of Cu. This phenomenon, already reported in the literature for acid-treated alloyed Pt-labile metal bimetallic catalysts,[34,62,63] produces materials with high surface area. Fig. S4 displays high-resolution images of the lattice fringes for the base and CS Pt_3Cu/C catalyst, along with the Fast-Fourier Transform, to estimate the *d*-spacing. An expansion in the *d*-spacing is observed after the Cu removal

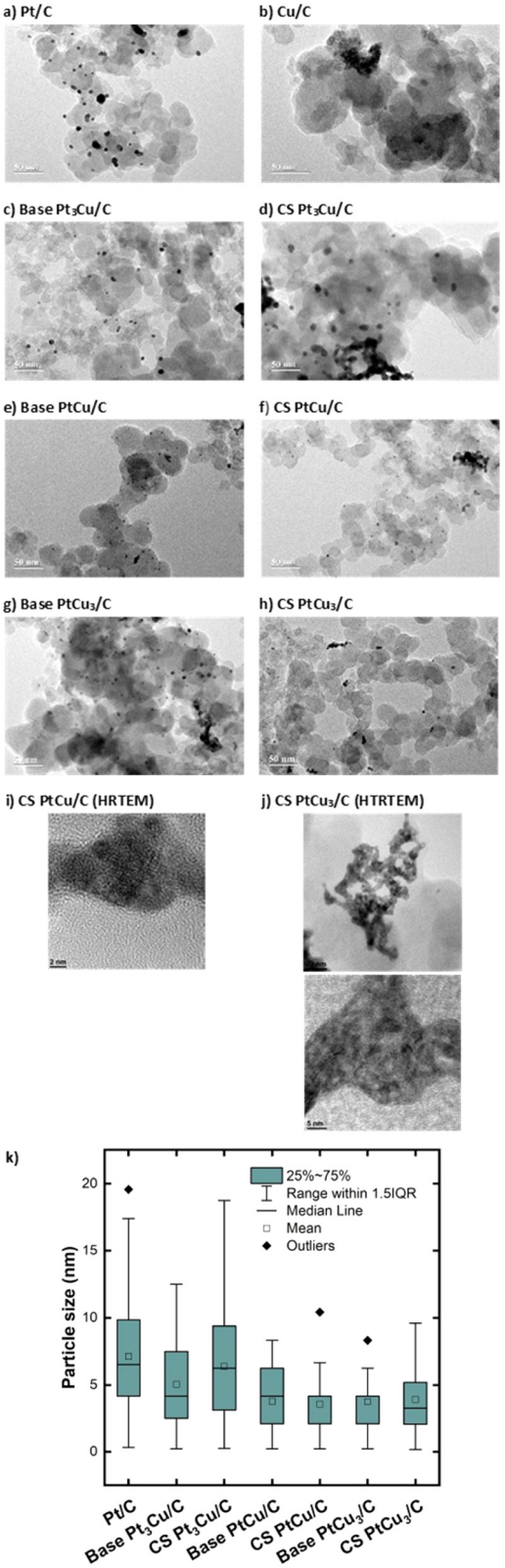

Fig. 4 (a)–(j) TEM images of the base and CS electrocatalysts and (k) statistical information from the particle size distribution (box plot for each material).

due to the rearrangement of the crystalline structure after the removal of the Cu atoms. Finally, to confirm the potential formation of a CS structure, Fig. S5 presents the EDS-STEM line mapping of the base and CS Pt_3Cu/C electrocatalysts (material with minor evidence of CS structure formation), along with the change in the Pt : Cu ratio with position. As observed, after the acid treatment, the CS material exhibits Pt enrichment due to the Cu lixiviation process, which is more pronounced on the edges of the nanoparticles. In this way, all the structural and morphological characterizations provide sufficient support to infer that the acid treatment leads to Pt-enriched CS structures.

3.2. Electrocatalytic performance assessment

Before presenting the electrochemical characterization, it is important to note that these measurements were performed on the candidate materials for the ethanol electroreformer, namely the CS materials, and Pt/C as the reference monometallic material. Cu/C is only shown in the blank voltammetries due to its negligible activity compared to Pt materials for CO stripping and EEO.

Fig. 5 shows the blank CV of these materials in 0.5 M H_2SO_4. CV is an important technique that can give an "electrochemical radiography" of the catalysts' surfaces. As can be seen, all the materials, except for Cu/C, present an analogous overall shape. In the case of Cu/C, there is an intense anodic peak *circa* 0.25 V *vs.* RHE with a soft drop up to 0.7 V. This process is ascribed to the oxidation of Cu(0)/Cu(I) species to Cu(II), as described in the literature.[35,64,65] The Pt/C displays the typical hydrogen adsorption/desorption region associated with the different crystalline facets (111, 110, and 100) between 0.05 and 0.35 V *vs.* RHE, in addition to the formation of PtOH above 0.8 V.[66] The CS materials maintain the general profile, although some changes are visible. The peaks associated with the different Pt crystalline facets in the H adsorption/desorption peaks are bigger but less defined or undefined. After the large Cu removal undergone by the CS materials, the created irregular Pt-enriched surface does not so clearly expose the typical 111, 110, and 100 facets. On the other hand, the CS $PtCu_3/C$, the material with the lowest metal loading, shows an intense double-layer contribution, likely due to the highest capacity contribution of the carbon support. Moreover, the current signal in the high potential region, corresponding to the oxygen adsorption/desorption, is more intense in the sequence CS $PtCu_3/C$ > CS PtCu/C > CS Pt_3Cu/C > Pt/C. This behavior can be attributed to the surface defects formed on the CS nanoparticles after acid treatment, which stimulates OH adsorption.[67,68] The variations observed between the bimetallic base and CS materials are shown and discussed in the SI (Fig. S6).

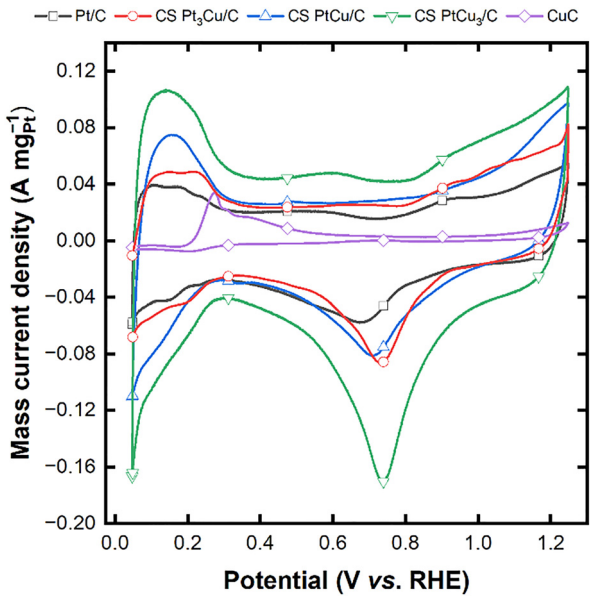

Fig. 5 Cyclic voltammetry (50 mV s^{-1}) of the electrocatalysts in 0.5 mol L^{-1} H_2SO_4.

Fig. S7 shows the CO-stripping profiles of the candidate materials, from which the electrochemically active surface area (EASA) can be estimated. Values are collected in Table 2. As can be seen, there is an increase in EASA as the Cu fraction in the initial materials increases. This tendency aligns with the CS TEM observation and further supports the formation of rougher, more irregular nanoparticle surfaces after Cu removal in the alloyed materials. In terms of the CO-stripping profiles, a progressive shift towards lower potentials of the onset potential with the increase of Cu content and a maximum current in the sequence CS $PtCu_3/C$ > CS PtCu/C > CS Pt_3Cu/C > Pt/C is observed. Additionally, previous activity is visualized in the CS materials, with the effect more pronounced as the initial Cu fraction increases, in the range of 0.3–0.7 V. This can be attributed to the aforementioned large number of oxyphilic surface defects,[67,69–71] in combination with eventual ox effects that weaken CO adsorption. These effects are more intense the higher the Cu fraction removed (CS $PtCu_3/C$ > CS PtCu/C > CS Pt_3Cu/C).

The ethanol electrochemical activity is displayed in Fig. 6a (mass normalized) and Fig. 6b (EASA normalized) for the anodic scans. The inset corresponds to the log plot of Fig. 6a, showing the stages at which the mass-normalized current density increases more significantly, providing an approximate indication of the onset potential. An overall sequence of CS $PtCu_3/C$ > CS PtCu/C > CS Pt_3Cu/C > Pt/C can be observed for the EEO activity. The Pt mass-normalized current densities, more influenced by the exposed surface area, show an evident beneficial effect of acid treatment. The EASA-normalized performance, which better reflects the intrinsic activity of the electrocatalysts, is also enhanced in the same sequence, reflecting the activation of the Pt active sites with the formation of the

Table 2 EASA obtained by the CO stripping for the different materials

Material	EASA/(m^2 g^{-1})
PtC	25.4
CS Pt_3Cu/C	40.0
CS PtCu/C	49.3
CS $PtCu_3/C$	73.1

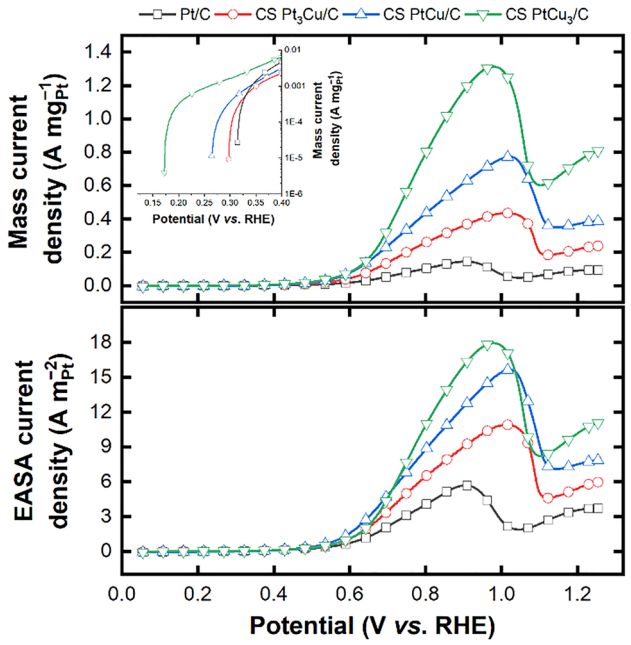

Fig. 6 EEO curves in the anodic scans (5 mV s^{-1}) in 1 mol L^{-1} H_3PO_4 and 5 mol L^{-1} ethanol for the different electrocatalysts.

CS structures. The expected decrease in the adsorption strength of the species formed during the EEO, combined with the presence of a large fraction of oxyphilic surface defects (oxygenated species are crucial for the EEO), results in a more active Pt surface that is less poisoned by the ethanolic adsorbates formed during the EEO. The interplay of these factors results in an increased turnover frequency, which contributes to the observed increase in activity. These effects are also visible in terms of the onset potential. Cathodic scans are presented and discussed in Fig. S8, and the chronoamperometric curves are shown in Fig. S9. The general trends reported for the CO-stripping and EEO curves are maintained in these figures. It must be noted that the proposed CS $PtCu_3$/C catalyst shows a peak mass current density of *ca.* 1.3 A mg_{Pt}^{-1}, which is among the highest values reported in the EEO literature review by Yang *et al.*[72] from CV data.

3.3. Electrolysis in high-temperature DEPEME

DEPEME results in the high-temperature electroreformer are presented in Fig. 7, expressed in terms of geometric area (a) and Pt mass (b). Moreover, the results for the commercial 20 wt% Pt/C are included for comparison purposes. As can be observed,

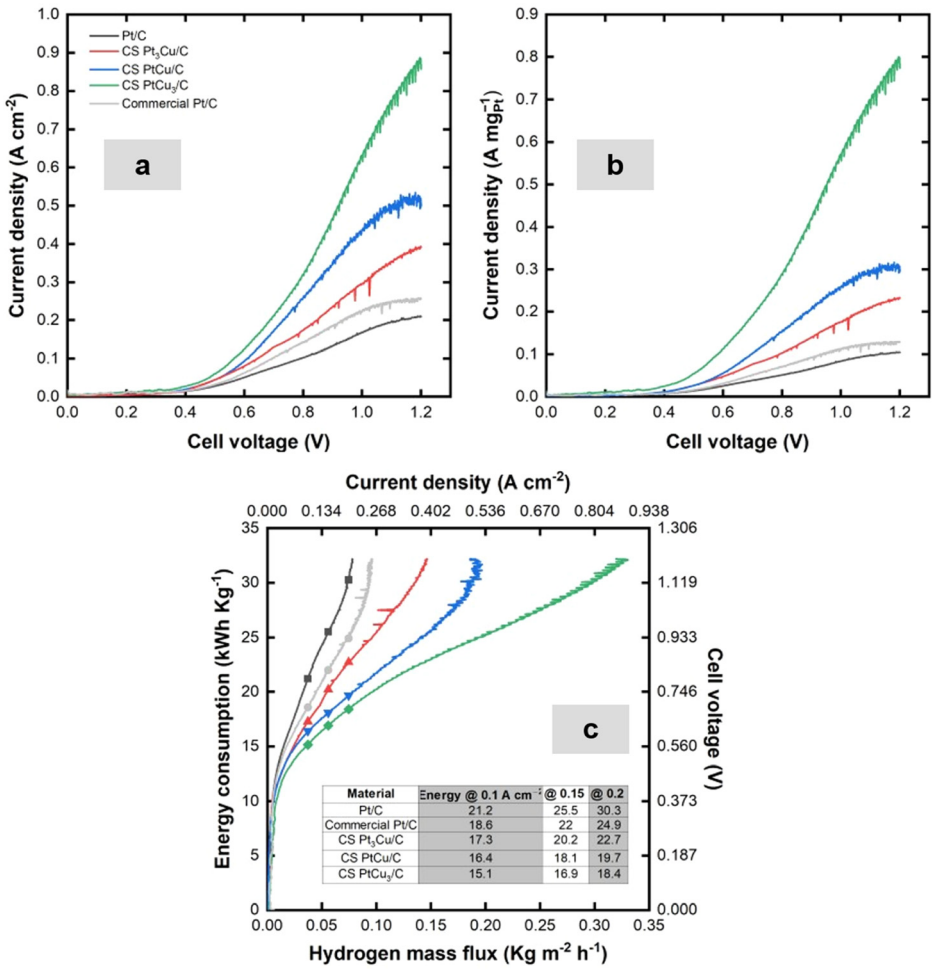

Fig. 7 Electrolysis curves for the high-temperature DEPEME at 150 °C based on: (a) electrode active area, (b) Pt mass; (c) energy requirements as a function of the H_2 produced (inset table: energy required (kWh kg^{-1} H_2) at 0.1, 0.15, and 0.2 A cm^{-2}).

the polarization curves, in both geometric area-based and Pt mass-based plots, match the tendencies shown in Fig. 6. The CS materials exhibit enhanced performance of the CS materials in the sequence CS $PtCu_3$/C > CS PtCu/C > CS Pt_3Cu/C, which outperform the Pt/C materials. Fig. 6c shows the energy demand as a function of the hydrogen produced. The hydrogen flux is calculated using Faraday's law, based on the 100% current efficiency measured for hydrogen production at the cathode. The energy demand per kg of H_2 was calculated from the polarization curves and the produced H_2.[73] As expected, there is a drop in the required energy when the CS materials are used, especially with the most active CS $PtCu_3$/C, due to the larger current and, thus, higher hydrogen production at a fixed cell voltage. The inset of Fig. 6c shows a table with the energy consumption at current densities of 0.1, 0.15, and 0.2 A cm^{-2}, which are reference values used in similar ethanol electrochemical reforming systems.[20,21,74–78] In the referred studies, ethanol electroreforming in liquid-fed Nafion®-based DEPEME demanded 15 to 30 kWh per kg of H_2 operating in equivalent current densities, while the energy consumption herein is only 15.1–18.4 kWh kg^{-1}. Finally, the energy demands in this study are lower than the approximately 50 kWh per kilogram of hydrogen reported for PEM water electrolysis (according to U.S. Department of Energy targets (2.0 A cm^{-2} at 1.9 V)).[79]

In comparison with similar high-temperature PBI-based PEM electrolyzers, to the authors' knowledge, only Aili *et al.*[80] reported the results of a high-temperature H_3PO_4-doped PBI-based PEM steam electrolysis, achieving a maximum performance of 0.6 A cm^{-2} at ≈1.8 V (48.2 kWh kg^{-1} of H_2). Instead, the CS $PtCu_3$/C would only demand 25 kWh kg^{-1} of H_2 operating at 0.6 A cm^{-2}, almost halving the required energy. Thus, regarding energy demand, DEPEME seems promising; nevertheless, it must be acknowledged that performance improvements are necessary to increase hydrogen production, aiming to match that of a water PEM electrolyzer.

Fig. 8 depicts the product distribution for the different electrocatalysts (Fig. 8a), and Fig. 8b displays the number of electrons (n, from eqn (6), where f is the molar fraction of each product) released per molecule of ethanol oxidized and H_2 yield. Given that hydrogen evolution is the sole reaction occurring in the cathode, the number of electrons released compared to the overall available (12) can be used to estimate the H_2 yield (Y_{H_2}) according to eqn (7).

$$n = \frac{2f_{\text{acetaldehyde}} + 4f_{\text{acetic acid}} + 6f_{CO_2}}{f_{\text{acetaldehyde}} + f_{\text{acetic acid}} + f_{CO_2}/2} \quad (6)$$

$$Y_{H_2} = n/12 \quad (7)$$

As can be seen, the CS materials exhibit a greater selectivity towards complete ethanol oxidation to carbon dioxide in the sequence CS $PtCu_3$/C > CS PtCu/C > CS Pt_3Cu/C. The acid treatment results in a surface with a large number of defects, including kinks, steps, and vacancies.[36,81–84] Such defects, which generate Pt atoms with low coordination numbers, are known to be more suitable for cleaving the C–C bond in the EEO. These, combined with the electronic effect and operation at high temperatures, can enable a CO_2 selectivity exceeding 50% for the CS $PtCu_3$/C material. Fig. S10 and, in particular, S11 illustrate a correlation between the presence of surface defects and CO_2 selectivity, including a more detailed discussion of the results. Additionally, the oxyphilic character of the surface defects results in a slightly higher percentage of acetic acid compared to the Pt/C materials, even though it is the least selective product. Furthermore, these OH species are required to complete the oxidation of the CH_x and CO species generated after the C–C cleavage. Its importance has also been highlighted in Fig. S11 through the inclusion of the CO onset potential. Such results lead to the utilization of almost 50% of the electrons available in the ethanol molecule, achieving a maximum of nearly 3 moles of H_2 per mole of ethanol. For instance, in the CS $PtCu_3$/C, the number of electrons varies between 4.5 and 6, corresponding to 2.25 to 3 mol of H_2 per mol of reacted ethanol, resulting in a H_2 yield of up to 50%. To complement this study, Fig. S12 presents a preliminary stability test conducted at 0.7 V for 6 h after running the polarization curves in a sequence of 5 consecutive days for the CS $PtCu_3$/C. As can be seen, there is a daily performance decay that nevertheless recovers the following day. This tendency has already been observed for high-temperature DEFC,[23,41] and is mainly attributed to the catalyst poisoning. During shutdown and start-up at open-circuit voltage, and the realization of the polarization curves, with the consequent voltage sweep, the adsorbed species can be desorbed, resulting in a cleaned surface that restarts a new poisoning cycle.

3.4. Techno-economic analysis for the implementation of a second-generation ethanol plant and high-temperature DEPEME

Given these encouraging results, a preliminary study is proposed to assess the potential of this technology for hydrogen production, for example, coupled with a sugar–ethanol plant. In this case, we consider the production of ethanol from the closest sugarcane plant to Brasilia (Jalles Machado, Goinesia, Goiás, Brazil). The leftover bagasse serves as a raw material for producing second-generation ethanol, which is intended for use in hydrogen production at the DEPEME. This hydrogen would be transferred to an ammonia plant to produce urea, which would be used to fertilize the sugarcane plantation. Table 3 shows a feasibility analysis based on mass balances, including the calculation sequence. The calculations are based on the annual ethanol production from sugarcane, as reported by the plant in 2023, and the specific production from sugarcane, which allows for estimating the required amount of sugarcane. Next, the specific area per ton of sugarcane is used to calculate the total planting area, which, combined with the specific urea needed, leads to the overall required urea.

Once we know the necessary urea, the required annual hydrogen can be calculated from the stoichiometries of the urea and ammonia syntheses. The key parameter to quantify the ethanol consumed in the DEPEME to produce the required hydrogen can be appraised from Fig. 8b. At 0.95 V and 0.55 A cm^{-2}, the average number of electrons produced in the EEO is 4.7, associated with a hydrogen production of 2.35 mols.

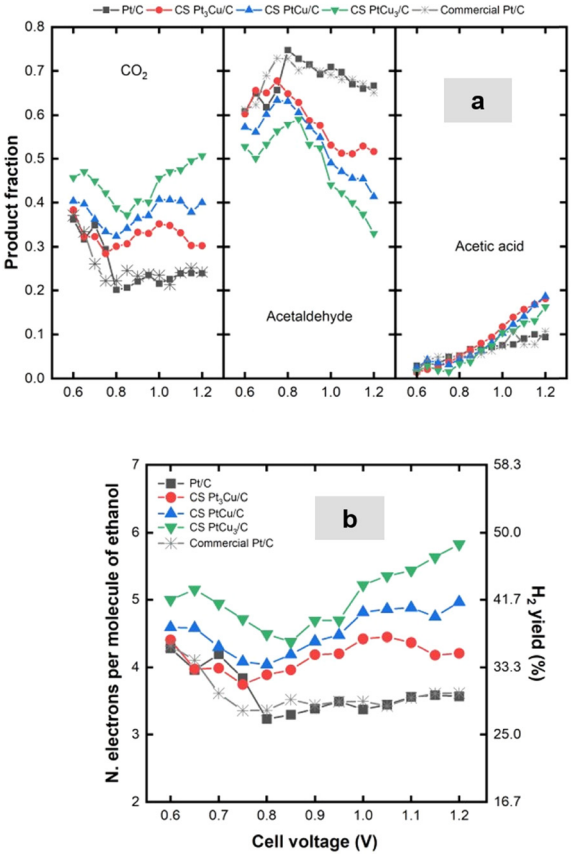

Fig. 8 (a) Product distribution for the different electrocatalysts at different cell voltages, and (b) number of electrons per molecule of ethanol and faradaic efficiency as a function of the cell voltage.

We can assess the required ethanol from this value, which is compared with the potential ethanol produced from bagasse. The potential bagasse rates this latter magnitude through the specific production of ethanol per ton of bagasse in a second-generation ethanol plant.

According to Table 3, the potential ethanol produced by implementing a second-generation ethanol plant could be used to generate the required hydrogen for producing ammonia and urea, which are needed to fertilize the 2023 sugarcane plantation. Specifically, only *ca.* 1.2% of the overall ethanol produced in the plant would be necessary to ensure the required H_2 generation through DEPEME.

Finally, a preliminary economic analysis of the high-temperature DEPEME technology is presented, including a comparison with the PEM water electrolysis (PEME). For the DEPEME, the results obtained in this study for CS $PtCu_3$/C serve as a basis for design calculations, whereas for the PEME, the bibliography is used for this purpose. Regarding the DEPEME, to date, no CAPEX and OPEX information is available. For this reason, certain assumptions are considered when making the DEPEME economic calculations. CAPEX of PEME is typically expressed as USD kW^{-1}. This estimation may distort the comparison between DEPEME and PEME, given the larger electrode area needed in DEPEME and the lower energy consumption. Instead, CAPEX estimation based on the electrode area would be more suitable (USD cm^{-2}). Moreover, PEME CAPEX estimations rely on the use of IrO_2 in the anode (loading of 1–3 mg cm^{-2}) and Pt/C in the cathode (Pt loading of 0.5 mg cm^{-2}), as well as a Nafion® membrane as the electrolyte.[92,93] According to Premetek (USA), an electrocatalyst supplier, 5 g of high surface area IrO_x (10–20 $m^2\ g^{-1}$) has a price of 1789.00 USD (https://premetek.com/product/irox-powder-conductive-surface-area-1020-m2-g/, accessed June 10, 2025), whereas 5 g of 20 wt% Pt/C costs 374.00 USD (https://premetek.com/product/20-pt-on-vulcan-xc-72/, accessed June 10, 2025). In DEPEME, both electrodes use Pt-based materials; in the cathode, 0.5 mg cm^{-2} of Pt from an analogous Pt/C material is typically used, so that we can consider the same economic basis; in the anode, for rough estimation, we can attribute most of the price to the Pt loading, neglecting the contributions of Cu and C. The Pt wt% in the $PtCu_3$/C is approximately 10, with a price of 298.00 USD (https://premetek.com/product/10-pt-on-vulcan-xc-72/, accessed June 10, 2025). Nevertheless, we can consider the value of 20 wt% Pt/C from a conservative approach, accounting for the contributions of Cu, C, and chemical treatments, 374.00 USD. The mass of 5 g of catalysts only provides 1 g of metal; therefore, for 5 g (the same reference mass used for IrO_x), the final value would be 1870.00 USD. Both values could be considered close enough to suggest similar specific prices (USD g^{-1}) for the electrocatalysts. Nafion® is the most extended proton exchange membrane used in PEME, whose price is >500.00 USD m^{-2}.[94] Our membrane is a H_3PO_4-doped PBI membrane, for which a reference value can be found from the Fuel Cell Store (https://www.fuelcellstore.com/celtec-p-membrane-82700100, accessed June 10, 2025) of 157 USD for a membrane of 0.064496 m^2. Applying the "0.6 rule" for the cost-curve costs,[95] we can estimate a value of 813 USD m^{-2}, which falls within the range of Nafion® membranes. Based on the proposed approaches, where the electrocatalysts and membranes have similar costs, we can use the PEME reference value from Peterson *et al.*[96] for DEPEME, as a function of the geometric area, 1.3 USD cm^{-2} for CAPEX estimation.

According to the literature,[97] the stack constitutes approximately 60% of the CAPEX of a PEME, with other contributions coming from the balance of plant (15%), H_2 conditioning (10%), and power electronics (15%). Although there may be variations between the PEME and DEPEME, due to the larger electrode area required by the DEPEME, some of the costs may compensate for each other; for instance, the balance of plant can be more expensive due to the higher size of the electrolyzer; however, the power electronics are cheaper given the reduced energy requirements of the DEPEME. Thereby, the other CAPEX contributions are considered equal for both systems. The OPEXs, excluding the cost of electricity, are estimated to be 5% of the CAPEX (with a typical range of 2–5%).[98–101] The cost of electricity was calculated based on the energy consumption of the electrolyzer. The considered price is obtained from the electricity company in the state of Goiás (Equatorial Goiás Distribuidora de Energia S.A., https://go.equatorialenergia.com.br/valor-de-tarifas-e-servicos/#demais-classes, accessed June 13th, 2025), ≈ 123.00 USD MWh^{-1}. This scenario leads to the results

Table 3 Estimation of the potential ethanol required to produce hydrogen, ammonia, and urea for fertilizing the entire sugarcane planting area, based on the annual ethanol production of the Jalles Machado sugar and ethanol plant in 2023

Parameter	Acronym	Amount	Unit	Source
Annual ethanol production	AEP	387	10^6 L year^{-1}	85
Specific production per ton of sugarcane	SPS	80	L ton^{-1}	86
Required tons of sugarcane	RTS	4.84	10^6 ton year^{-1}	AEP/SPS
Specific sugarcane per hectare of plants	SSHP	78.7	ton ha^{-1} year^{-1}	87
Required hectares of sugarcane	RHS	61 452	ha	RTS/SSHP
Required urea per hectare of sugarcane	RUHS	200	kg ha^{-1}	88
Required urea	RU	12.3	10^3 ton	RHSxRUHS
Overall urea production: $2NH_3 + CO_2 \rightleftharpoons NH_2CONH_2 + H_2O$				
Molar proportion urea : ammonia		0.5		
Mass proportion urea : ammonia	MPUA	1.763		
Required ammonia	RA	6.97	10^3 ton	RU/MPUA
Overall ammonia production: $N_2 + 2H_2 \rightleftharpoons NH_3$				
Molar proportion ammonia : hydrogen		0.5		
Mass proportion ammonia : hydrogen	MPAH	8.515		
Required hydrogen	RH	819	ton	RA/MPAH
Operating factor	OF	8000	h year^{-1}	89
Hourly hydrogen consumption (in 1 year)	HHC	102.3	kg h^{-1}	RH/OF
Operation at 0.95 V and 0.55 A cm^{-2}. In this condition, the required energy consumption is ≈25 kWh kg^{-1} of H_2, half of PEM water electrolysis				
H_2/ethanol proportion (according to Fig. 8b)		2.35		
Mass proportion H_2 : ethanol	MPEH	0.102		
Hourly ethanol consumption	HEC	1005	kg h^{-1}	HHC/MPEH
Ethanol density	ED	789	kg m^{-3}	
Annual required ethanol for producing urea to fertilize the sugarcane planting		**3.99**	10^3 m^3 year^{-1}	(HEC/ED) × OF
Bagasse obtained per ton of sugarcane	BOTS	0.3	ton ton^{-1}	90
Obtained bagasse	OB	1.45	10^6 ton year^{-1}	RTSxBOTS
Specific production of ethanol per ton of bagasse	SPEB	0.232	m^3 ton^{-1}	91
Potential ethanol to be produced		**336.6**	10^3 m^3 year^{-1}	OB × SPEB

summarized in Table 4. CAPEX annualization is calculated considering a lifetime of 10 years (expected for PEME, not available to date for DEPEME, so the same lifetime expectation is initially assumed) and an interest rate of 15%, resulting in an annual capital charge ratio (ACCR) of 0.199.[102]

As shown in Table 4, under the described scenario, the DEPEME option is more economical than the PEME, primarily due to the higher electricity costs. The estimated total cost, comprising CAPEX, OPEX, and electricity, would be 4.47 and 5.87 MUSD year^{-1} for DEPEME and PEME, respectively. Although some assumptions may affect the accuracy of the calculations, the developed tool allows us to observe interesting trends that can be better evaluated through a sensitivity analysis. Fig. 9 shows the evolution of the total costs as a function of the specific stack CAPEX and the price of electricity.

The DEPEME becomes more onerous than the PEME when the specific stack CAPEX increases due to the required larger area than the PEME. On the other hand, the PEME is the most expensive option when electricity prices are high, as it is more energy-demanding due to its operation at higher cell voltages. This tool can also simulate other conditions, such as varying cell voltages and current densities, enabling the assessment of the impact of improvements on both systems. Furthermore, the system's lifetime can also be evaluated by changing the ACCR, a parameter that increases with a minor lifetime expectancy. These parameters are simulated in Fig. S13.

In addition to the electroreformer, the DEPEME also requires a separation sequence to obtain the oxidation product (acetaldehyde and, to a lesser extent, acetic acid), which can generate revenues from their sale. Furthermore, the unreacted ethanol and water can be recycled, thereby reducing the demand for these resources. Fig. S14–S16 and Tables S3–S10 display the sequence of calculations performed to estimate the benefit margin in the case of separating the acetaldehyde and acetic acid formed. As can be seen, a significant benefit margin appears after the inclusion of the separation sequence, which can indeed compensate for the high CAPEX demanded for the DEPEME. It is essential to note that this part of the study focuses solely on the fractionation columns, along with an activated carbon fixed-bed adsorber, to retain the acetic acid formed during the process. Furthermore, in the case of DEPEME, a vaporizer is necessary, which will consequently increase energy requirements. This vaporizer would undoubtedly increase the system's CAPEX and OPEX. Notwithstanding, the possibility of heat integration, such as preheating the feed stream to the DEPEME,[103,104] is expected to reduce the energy requirements (see the proposed process flow diagram in Fig. S14, which includes heat integration). In any case, this economic evaluation must be considered in preliminary terms to visualize the influence of relevant parameters such as the cost of the electrolyzer, electricity, lifetime, and operating conditions, among others. Alcohol electrochemical reforming requires more maturity to provide more solid techno-economic data, especially addressing long-term performance and actual estimations of CAPEX and OPEX. Nonetheless, the results are rather promising, considering there is room for improvement in DEPEME performance, which would produce more H_2 at a lower cost. Fig. S17 and Table S11 present the calculations for

Table 4 Description and presentation of the economic scenario for the total costs of the DEPEME and PEME

Parameter				Value			Units
According to Table 3, the required hourly demand of H_2 is				102.31			kg h^{-1}
Proposed ethanol electroreformer				**Water electrolyzer**			
Cell voltage	0.95	V	From polarization curves	Cell voltage	1.9	V	
Current density	0.55	A cm^{-2}		Current density	2	A cm^{-2}	
Hydrogen production rate	0.205	kg H_2 m^{-2} h^{-1}		Hydrogen production rate	0.746	kg H_2 m^{-2} h^{-1}	
Required electrolyzer area	498.6	m^2		Required electrolyzer area	137.1	m^2	
Power	2.60	MW		Power	5.21	MW	
Specific consumed energy	25.46	kWh kg^{-1} H_2		Specific consumed energy	50.92	kWh kg^{-1} H_2	
Annual energy demand	20 839.58	MWh		Annual energy demand	41679.16	MWh	
Specific stack CAPEX	1.3	USD cm^{-2}		Specific stack CAPEX	1.3	USD cm^{-2}	
Stack CAPEX	6.48	MUSD		Stack CAPEX	1.782	MUSD	60% of the total CAPEX
Other components (balance of plant, gas conditioning, power electronics)	1.188	MUSD	Equal to PEME	Other components (balance of plant, gas conditioning, power electronics)	1.188	MUSD	40% remaining
Total CAPEX	7.67	MUSD		Total CAPEX	2.971	MUSD	
To annualize the CAPEX, we consider a lifetime of 10 years (same as PEME, though there is no experimental data)				To annualize the CAPEX, we consider a lifetime of 10 years			
Annual capital charge ratio (ACCR)	0.199			Annual capital charge ratio (ACCR)	0.199		
Annualized CAPEX	1.526	MUSD $year^{-1}$		Annualized CAPEX	0.591	MUSD $year^{-1}$	
OPEX (not including electricity)	0.383	MUSD $year^{-1}$	5% of the total CAPEX	OPEX (not including electricity)	0.149	MUSD $year^{-1}$	5% of the total CAPEX
Electricity price	123	USD MWh^{-1}	Reference of the energy company in Goiás (BR)	Electricity price	123	USD MWh^{-1}	Reference of the energy company in Goiás (BR)
Electricity cost	2.563	MUSD $year^{-1}$		Electricity cost	5.127	MUSD $year^{-1}$	
OPEX + CAPEX + ELECTRICITY COSTS ("TOTAL COSTS")	**4.47**	**MUSD $year^{-1}$**		**OPEX + CAPEX + ELECTRICITY COSTS ("TOTAL COSTS")**	**5.87**	**MUSD $year^{-1}$**	

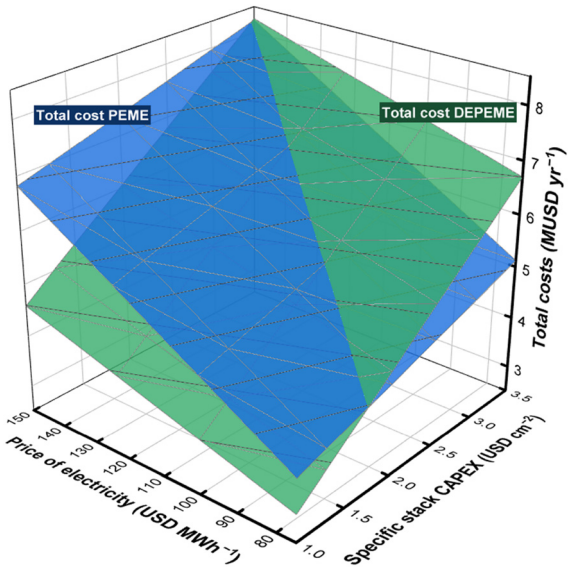

Fig. 9 Evolution of the total costs depending on the price of electricity and specific stack CAPEX.

estimating the system efficiency and the excess energy applied to the DEPEME, PEM water electrolyzer, and solid oxide water electrolyzer. The results demonstrate two contradictory results for the DEPEME compared to the water electrolysis: (i) the significant excess of energy required in the DEPEME compared to the theoretical one, which is primarily attributed to the sluggishness of the EEO kinetics, as a negative part; (ii) the highest transferred energy efficiency from the fuel to H_2, due to the energy provided by the ethanol combustion, which contribute to drastically reduce the energy demand of the DEPEME comparted to the water electrolyzers.

4. Conclusions

CS PtCu materials can be prepared from the acid treatment of partially alloyed PtCu/C materials. With this procedure, nanosized particles are obtained with a structure of Pt-enriched shells on alloyed PtCu cores, which becomes more evident as the Cu fraction in the base material increases. This CS structure renders materials with a higher surface area, enhanced CO tolerance, and higher EEO activity (higher current densities and lower onset potentials) in the sequence CS $PtCu_3$/C > CS PtCu/C > CS Pt_3Cu/C compared to Pt/C, probably due to a combination of structural (surface defects generated during the Cu removal of the shell) and electronic effects (alloyed PtCu in the core structure). Such a scenario enhances the high-temperature H_3PO_4-doped DEPEME performance, yielding higher amounts of hydrogen (*circa* 50%) per mol of ethanol and a CO_2 selectivity of nearly 50% for the best CS $PtCu_3$/C, which is significantly higher than that of Pt/C. Based on the results of this latter catalyst, preliminary techno-economic calculations have demonstrated the potential of this technology to produce hydrogen at low costs (*vs.* a conventional PEM water electrolyzer), with room for improvements to reduce them further, from the expected improved maturity as more R&D is implemented in the area (further enhanced performances, lifetime tests, better estimation of CAPEX and OPEX, among others).

5. Future directions/perspectives

For future studies, given the relevance of long-term cell performance stability for real-world applications, lifetime analyses with extended durations are crucial, either under steady (fixed current or cell voltage) or dynamic (variable current or cell voltage) loads. Indeed, such a challenge is established as a goal by the Department of Energy,[79] and any potential decay must be analyzed in detail, with solutions proposed to address this apparent DEPEME challenge.

Author contributions

Conceptualization: R. C. and J. J. L.; data curation: D. F. P., R. C., J. G. C., A. C. and J. J. L.; formal analysis: J. G. C, A. C. and J. J. L.; funding acquisition: J. G. C, A. C. and J. J. L.; investigation: D. F. P., J. G. C., A. C. and J. J. L.; methodology: D. F. P., R. C., J. G. C., A. C. and J. J. L.; project administration: J. J. L.; resources: R. C., J. G. C., A. C. and J. J. L.; supervision: R. C. and J. J. L.; validation: R. C. and J. J. L.; visualization/writing – original draft/writing – review & editing J. G. C., A. C. and J. J. L.

Conflicts of interest

There are no conflicts to declare.

Data availability

The authors confirm that the data supporting the findings of this study are available within the article and its supplementary information (SI). Supplementary information: Experimental results on XPS, particle size distribution by TEM, high resolution TEM and FFT, EDS-STEM, CV on supporting electrolyte, electrochemical CO stripping, CV and CA in EEO conditions, analysis of surface defect from XRD, preliminary lifetime analysis, complementary techno-economic analysis, simulation and design of the DEPEME, including the separation of the products formed by the EEO, the design and economic evaluation of these equipments, economic profitability including the EEO products, and a final comparison of efficiencies with PEM and SO water electrolyzers. See DOI: **https://doi.org/10.1039/d5ey00210a**.

Acknowledgements

The authors thank Coordenação de Aperfeiçoamento de Pessoal de Nível Superior (CAPES) for a scholarship awarded to Rudy Crisafulli. In addition, we acknowledge the research scholarship provided by CNPq, FAPDF (process no. 0193.001.473/2017), and FINEP through the DENDEPALM

project. Finally, the authors thank the University of Brasilia for the financial support for publishing this manuscript.

Notes and references

1 P. Bains, S. Bennet, L. Collina, E. Connelly, C. Delmastro, S. Evangelopoulou, M. Fajardy, A. Gouy, J. B. Le Marois, P. Levi, R. Martinez Gordon, S. McDonagh, F. Pavan, A. Pizarro, N. Sloots and C. Winkler, in *Global Hydrogen Review 2023*, ed. T. Gül, U. Remme and J. M. Bermudez Menendez, International Energy Agency, Paris, France, 2023.
2 S. K. Dash, S. Chakraborty and D. Elangovan, *Energies*, 2023, **16**, 1141.
3 Z. Abdin, A. Zafaranloo, A. Rafiee, W. Mérida, W. Lipiński and K. R. Khalilpour, *Renewable Sustainable Energy Rev.*, 2020, **120**, 109620.
4 International Energy Agency, *Global Hydrogen Review 2024*, International Energy Agency, Paris, France, 2024.
5 M. Tao, J. A. Azzolini, E. B. Stechel, K. E. Ayers and T. I. Valdez, *J. Electrochem. Soc.*, 2022, **169**, 054503.
6 C. Dolle, N. Neha and C. Coutanceau, *Curr. Opin. Electrochem.*, 2022, **31**, 100841.
7 H. A. Miller, F. Vizza and P. Fornasiero, in *Nanotechnology in Catalysis*, ed. M. Van De Voorde and B. Sels, Wiley, 1st edn, 2017, pp. 961–978.
8 H. A. Miller, A. Lavacchi and F. Vizza, *Curr. Opin. Electrochem.*, 2020, **21**, 140–145.
9 D. M. De Araujo, I. D. Barbosa Segundo, J. C. Cardozo, J. E. L. Santos, J. H. O. Nascimento, A. D. Gondim, E. V. Dos Santos and C. A. Martínez-Huitle, *Fuel*, 2024, **373**, 132369.
10 H. L. Oliveira, J. E. L. Santos, A. D. Gondim, L. N. Cavalcanti, F. Correia De Carvalho, S. S. L. Castro, C. A. Martínez-Huitle and E. V. Dos Santos, *Electrochim. Acta*, 2024, **499**, 144692.
11 R. Núñez, N. Merayo, D. Hermosilla, A. Gascó, A. J. Dos santos-García and Á. Caravaca, *Curr. Opin. Electrochem.*, 2024, **46**, 101533.
12 E. Bertrand and C.-G. Dussap, in *Liquid Biofuels: Bioethanol*, ed. C. R. Soccol, G. Amarante Guimarães Pereira, C.-G. Dussap and L. Porto De Souza Vandenberghe, Springer International Publishing, Cham, 2022, vol. 12, pp. 1–12.
13 M. O. S. Dias, M. P. Cunha, C. D. F. Jesus, G. J. M. Rocha, J. G. C. Pradella, C. E. V. Rossell, R. Maciel Filho and A. Bonomi, *Bioresour. Technol.*, 2011, **102**, 8964–8971.
14 D. De, C. L. E. Penalva Santos, C. Correa, Y. Amaral Alves, C. Gomes Souza and R. A. Mancebo Boloy, *Alexandria Eng. J.*, 2023, **67**, 153–170.
15 V. Bambagioni, M. Bevilacqua, C. Bianchini, J. Filippi, A. Lavacchi, A. Marchionni, F. Vizza and P. K. Shen, *ChemSusChem*, 2010, **3**, 851–855.
16 E. Ruiz-López, E. Amores, A. Raquel De La Osa, F. Dorado and A. De Lucas-Consuegra, *Chem. Eng. J.*, 2020, **379**, 122289.
17 M. Bellini, M. V. Pagliaro, A. Marchionni, J. Filippi, H. A. Miller, M. Bevilacqua, A. Lavacchi, W. Oberhauser, J. Mahmoudian, M. Innocenti, P. Fornasiero and F. Vizza, *Inorg. Chim. Acta*, 2021, **518**, 120245.
18 Y. X. Chen, A. Lavacchi, H. A. Miller, M. Bevilacqua, J. Filippi, M. Innocenti, A. Marchionni, W. Oberhauser, L. Wang and F. Vizza, *Nat. Commun.*, 2014, **5**, 4036.
19 A. Rodríguez-Gómez, F. Dorado, A. De Lucas-Consuegra, P. Sánchez and A. R. De La Osa, *Catal. Today*, 2024, **427**, 114411.
20 J. Serrano-Jiménez, A. R. De La Osa, A. Rodríguez-Gómez, P. Sánchez, A. Romero and A. De Lucas-Consuegra, *J. Environ. Chem. Eng.*, 2023, **11**, 109703.
21 C. Lo Vecchio, E. Mosca, S. Trocino and V. Baglio, *Catalysts*, 2024, **14**, 415.
22 A. Caravaca, F. M. Sapountzi, A. De Lucas-Consuegra, C. Molina-Mora, F. Dorado and J. L. Valverde, *Int. J. Hydrogen Energy*, 2012, **37**, 9504–9513.
23 A. Caravaca, A. De Lucas-Consuegra, A. B. Calcerrada, J. Lobato, J. L. Valverde and F. Dorado, *Appl. Catal., B*, 2013, **134–135**, 302–309.
24 L. Qiang, W. Wen, Q. Yan, P. Zhao, J. Ma, C. Liu, M. Zhao, Y. He, H. Xiao and J. Jia, *J. Alloys Compd.*, 2024, **1001**, 175120.
25 L. Eswaraditya Reddy, D. Gollapudi, G. Mahnot Jain, S. Kolluru and G. V. Ramesh, *Mater. Today: Proc.*, 2023, **92**, 636–641.
26 C. Liang, R. Zhao, T. Chen, Y. Luo, J. Hu, P. Qi and W. Ding, *Adv. Sci.*, 2024, **11**, 2308958.
27 B. Alves, D. De Paula, R. Crisafully and J. J. Linares, *J. Braz. Chem. Soc.*, 2022, **33**(11), 1342–1351.
28 J. J. Linares, S. C. Zignani, T. A. Rocha and E. R. Gonzalez, *J. Appl. Electrochem.*, 2013, **43**, 147–158.
29 Q. Li, R. He, J. O. Jensen and N. J. Bjerrum, *Fuel Cells*, 2004, **4**, 147–159.
30 E. Berretti, L. Osmieri, V. Baglio, H. A. Miller, J. Filippi, F. Vizza, M. Santamaria, S. Specchia, C. Santoro and A. Lavacchi, *Electrochem. Energy Rev.*, 2023, **6**, 30.
31 Y. Xu, S. Cai, B. Chi and Z. Tu, *Int. J. Hydrogen Energy*, 2024, **50**, 548–591.
32 J. J. Linares, T. A. Rocha, S. Zignani, V. A. Paganin and E. R. Gonzalez, *Int. J. Hydrogen Energy*, 2013, **38**, 620–630.
33 K. Artyushkova, B. Halevi, M. Padilla, P. Atanassov and E. A. Baranova, *J. Electrochem. Soc.*, 2015, **162**, H345–H351.
34 V. S. Saji, *Int. J. Hydrogen Energy*, 2024, **60**, 1077–1091.
35 M. Ammam and E. B. Easton, *J. Power Sources*, 2013, **222**, 79–87.
36 M. Huang, Y. Jiang, C. Jin, J. Ren, Z. Zhou and L. Guan, *Electrochim. Acta*, 2014, **125**, 29–37.
37 R. M. Castagna, J. M. Sieben, A. E. Alvarez and M. M. E. Duarte, *Int. J. Hydrogen Energy*, 2019, **44**, 5970–5982.
38 Y. Li, L. Guo, M. Du, C. Tian, G. Zhao, Z. Liu, Z. Liang, K. Hou, J. Chen, X. Liu, L. Jiang, B. Nan and L. Li, *Nat. Commun.*, 2024, **15**, 5598.
39 J. Végh, *J. Electron Spectrosc. Relat. Phenom.*, 2006, **151**, 159–164.
40 E. N. E. Sawy and V. I. Birss, *J. Electrochem. Soc.*, 2017, **164**, F1572–F1579.

41 J. Lobato, P. Cañizares, M. A. Rodrigo and J. J. Linares, *Fuel Cells*, 2009, **9**, 597–604.
42 S. Geng, J. González-Cobos, L. Pérez-Carcelén, V. Blanco-Gutiérrez, C. Marini, A. J. Dos Santos-García and Á. Caravaca, *Appl. Catal., B*, 2025, **365**, 124947.
43 R. Crisafulli, V. V. S. De Barros, F. E. Rodrigues De Oliveira, T. De Araújo Rocha, S. Zignani, L. Spadaro, A. Palella, J. A. Dias and J. J. Linares, *Appl. Catal., B*, 2018, **236**, 36–44.
44 K. Beliaeva, N. Grimaldos-Osorio, E. Ruiz-López, L. Burel, P. Vernoux and A. Caravaca, *Int. J. Hydrogen Energy*, 2021, **46**, 35752–35764.
45 W. Kang, R. Li, D. Wei, S. Xu, S. Wei and H. Li, *RSC Adv.*, 2015, **5**, 94210–94215.
46 R. Crisafulli, V. V. S. De Barros, F. E. Rodrigues De Oliveira, T. De Araújo Rocha, S. Zignani, L. Spadaro, A. Palella, J. A. Dias and J. J. Linares, *Appl. Catal., B*, 2018, **236**, 36–44.
47 R. Crisafulli, D. F. De Paula, S. C. Zignani, L. Spadaro, A. Palella, S. Boninelli, J. A. Dias and J. J. Linares, *Catalysts*, 2022, **12**, 1639.
48 X. Zhao, Q. Liu, Q. Li, L. Chen, L. Mao, H. Wang and S. Chen, *Chem. Eng. J.*, 2020, **400**, 125744.
49 I. Khalakhan, M. Vorokhta, X. Xie, L. Piliai and I. Matolínová, *J. Electron Spectrosc. Relat. Phenom.*, 2021, **246**, 147027.
50 I. A. Khan, Y. Qian, A. Badshah, D. Zhao and M. A. Nadeem, *ACS Appl. Mater. Interfaces*, 2016, **8**, 20793–20801.
51 M. Gong, D. Xiao, Z. Deng, R. Zhang, W. Xia, T. Zhao, X. Liu, T. Shen, Y. Hu, Y. Lu, X. Zhao, H. Xin and D. Wang, *Appl. Catal., B*, 2021, **282**, 119617.
52 B. Wu, J. Xiao, L. Li, T. Hu, M. Qiu, D. Lützenkirchen-Hecht, K. Yuan and Y. Chen, *CCS Chem.*, 2023, **5**, 2545–2556.
53 J. Zhang, P. Liang, X. Xu, R. Wang, S. Liu, C. Wang, B. Liu, L. Luo, M. Jin, H. Liu, H. Yi and S.-Y. Lu, *Nano Mater. Sci.*, 2024, S2589965124000242.
54 H. Li, C. Ren, S. Xu, L. Wang, Q. Yue, R. Li, Y. Zhang, Q. Xue and J. Liu, *J. Mater. Chem. A*, 2015, **3**, 5850–5858.
55 H. Xiang, Y. Zheng, Y. Sun, T. Guo, P. Zhang, W. Li, S. Kong, M. Ouzounian, H. Chen, H. Li, T. S. Hu, G. Yu, Y. Feng and S. Liu, *Nanoscale Adv.*, 2020, **2**, 1603–1612.
56 Z. Xiao, H. Wu, H. Zhong, A. Abdelhafiz and J. Zeng, *Nanoscale*, 2021, **13**, 13896–13904.
57 M. Kalyva, M. F. Sunding, A. E. Gunnæs, S. Diplas and E. A. Redekop, *Appl. Surf. Sci.*, 2020, **532**, 147369.
58 M. Wakisaka, S. Mitsui, Y. Hirose, K. Kawashima, H. Uchida and M. Watanabe, *J. Phys. Chem. B*, 2006, **110**, 23489–23496.
59 M. Weinert and R. E. Watson, *Phys. Rev. B: Condens. Matter Mater. Phys.*, 1995, **51**, 17168–17180.
60 Y.-S. Lee, K.-Y. Lim, Y.-D. Chung, C.-N. Whang and Y. Jeon, *Surf. Interface Anal.*, 2000, **30**, 475–478.
61 T. Gentil, V. Pinheiro, E. Paz, F. Souza, L. Parreira and M. Santos, *J. Braz. Chem. Soc.*, 2019, **30**(8), 1634–1646.
62 Y. Qiao, M. Peng, J. Lan, K. Jiang, D. Chen and Y. Tan, *J. Mater. Chem. A*, 2023, **11**, 495–511.
63 G. G. Li, E. Villarreal, Q. Zhang, T. Zheng, J.-J. Zhu and H. Wang, *ACS Appl. Mater. Interfaces*, 2016, **8**, 23920–23931.
64 M. Wu, X. Wu, L. Zhang, A. Abdelhafiz, I. Chang, C. Qu, Y. Jiang, J. Zeng and F. Alamgir, *Electrochim. Acta*, 2019, **306**, 167–174.
65 T.-H. Tsai, T.-W. Chen and S.-M. Chen, *Int. J. Electrochem. Sci.*, 2011, **6**, 4628–4637.
66 G. Jerkiewicz, *Electrocatalysis*, 2010, **1**, 179–199.
67 Z. Zhou, Z. Huang, D. Chen, Q. Wang, N. Tian and S. Sun, *Angew. Chem., Int. Ed.*, 2010, **49**, 411–414.
68 K.-S. Ju, I.-H. Jang, Y.-A. Choe, S.-C. Ri, H.-T. Pak and S.-O. Hong, *RSC Adv.*, 2023, **13**, 448–455.
69 G. Caballero-Manrique, A. Velázquez-Palenzuela, E. Brillas, F. Centellas, J. A. Garrido, R. M. Rodríguez and P.-L. Cabot, *Int. J. Hydrogen Energy*, 2014, **39**, 12859–12869.
70 G. Caballero-Manrique, J. Garcia-Cardona, E. Brillas, J. A. Jaén, J. M. Sánchez and P. L. Cabot, *Catalysts*, 2020, **10**, 563.
71 A. López-Cudero, A. Cuesta and C. Gutiérrez, *J. Electroanal. Chem.*, 2005, **579**, 1–12.
72 G. Yang, Q. Zhang, H. Yu and F. Peng, *Particuology*, 2021, **58**, 169–186.
73 J. De Paula, D. Nascimento and J. J. Linares, *J. Appl. Electrochem.*, 2015, **45**, 689–700.
74 J. Serrano-Jiménez, A. De Lucas-Consuegra, P. Sánchez, A. Romero and A. R. De La Osa, *Fuel*, 2023, **350**, 128728.
75 A. Rodríguez-Gómez, E. Lepre, F. Dorado, L. Sanchez-Silva, N. Lopez-Salas and A. R. De La Osa, *Mater. Today Energy*, 2023, **32**, 101231.
76 J. Serrano-Jiménez, A. R. De La Osa, A. Rodríguez-Gómez, P. Sánchez, A. Romero and A. De Lucas-Consuegra, *J. Electroanal. Chem.*, 2022, **921**, 116680.
77 A. Rodríguez-Gómez, F. Dorado, P. Sánchez and A. R. De La Osa, *J. Energy Chem.*, 2022, **70**, 394–406.
78 E. Ruiz-López, F. Dorado and A. De Lucas-Consuegra, in *Recent Advances in Electrochemical Promotion of Catalysis*, ed. P. Vernoux and C. G. Vayenas, Springer International Publishing, Cham, 2023, vol. 61, pp. 269–301.
79 Department of Energy, Technical Targets for Proton Exchange Membrane Electrolysis, **https://www.energy.gov/eere/fuelcells/technical-targets-proton-exchange-membrane-electrolysis**, (accessed November 25, 2024).
80 D. Aili, M. K. Hansen, C. Pan, Q. Li, E. Christensen, J. O. Jensen and N. J. Bjerrum, *Int. J. Hydrogen Energy*, 2011, **36**, 6985–6993.
81 V. Del Colle, A. Berná, G. Tremiliosi-Filho, E. Herrero and J. M. Feliu, *Phys. Chem. Chem. Phys.*, 2008, **10**, 3766.
82 F. Colmati, G. Tremiliosi-Filho, E. R. Gonzalez, A. Berná, E. Herrero and J. M. Feliu, *Phys. Chem. Chem. Phys.*, 2009, **11**, 9114.
83 A. Ferre-Vilaplana, C. Buso-Rogero, J. M. Feliu and E. Herrero, *J. Phys. Chem. C*, 2016, **120**, 11590–11597.
84 M. R. Zamanzad Ghavidel, A. H. A. Monteverde Videla, S. Specchia and E. B. Easton, *Electrochim. Acta*, 2017, **230**, 58–72.
85 Novacana, Jalles encerra 2023/24 com moagem de 7,35 mi de toneladas e produção recorde de açúcar, **https://www.novacana.com/noticias/jalles-encerra-2023-24-moagem-7-35-mi-toneladas-producao-recorde-acucar-221123**, (accessed November 28, 2024).

86 I. Baima Ferreira Freitas, C. Aparecida De Menezes and E. Luiz Silva, *Fuel*, 2020, **260**, 116419.
87 H. Thiemi, *Sugar Semi-annual*, United States Department of Agriculture, 2023.
88 G. C. Vitti and P. H. de Cerqueira Luz, *Nutrição e Adubação da Cana-de-Açúcar*, Rio de Janeiro (Brazil), 2009, **https://www.cetem.gov.br/antigo/agrominerais/livros/CanaAcucar.pdf**.
89 J. R. Couper, W. Roy Penney, J. R. Fair and S. M. Walas, *Chemical Process Equipment*, Elsevier, 2005, pp. 1–16.
90 P. Khatri and A. B. Pandit, *Biomass Bioenergy*, 2022, **158**, 106365.
91 A. K. Chandel, J. Q. Albarelli, D. T. Santos, S. P. Chundawat, M. Puri and M. A. A. Meireles, *Biofuels, Bioprod. Biorefin.*, 2019, **13**, 994–1014.
92 H. Yu, L. Bonville, J. Jankovic and R. Maric, *Appl. Catal., B*, 2020, **260**, 118194.
93 K. W. Ahmed, M. J. Jang, M. G. Park, Z. Chen and M. Fowler, *Electrochem*, 2022, **3**, 581–612.
94 S. Ahmad, T. Nawaz, A. Ali, M. F. Orhan, A. Samreen and A. M. Kannan, *Int. J. Hydrogen Energy*, 2022, **47**, 19086–19131.
95 G. Towler and R. Sinnott, *Chemical Engineering Design*, Elsevier, 2022, pp. 239–278.
96 D. Peterson, J. Vickers and D. DeSantis, *Hydrogen Production Cost From PEM Electrolysis*, Department of Energy, United States, 2020.
97 U. Babic, M. Suermann, F. N. Büchi, L. Gubler and T. J. Schmidt, *J. Electrochem. Soc.*, 2017, **164**, F387–F399.
98 KPMG, *How to evaluate the cost of the green hydrogen business case?* London, United Kingdom, 2022.
99 S. Shanian and O. Savadogo, *Discovery Energy*, 2024, **4**, 23.
100 A. Buttler and H. Spliethoff, *Renewable Sustainable Energy Rev.*, 2018, **82**, 2440–2454.
101 T. Egeland-Eriksen, J. F. Jensen, Ø. Ulleberg and S. Sartori, *Int. J. Hydrogen Energy*, 2023, **48**, 28712–28732.
102 G. Towler and R. Sinnott, *Chemical Engineering Design*, Elsevier, 2022, pp. 305–337.
103 H. Q. Nguyen and B. Shabani, *Energy Convers. Manage.*, 2020, **204**, 112328.
104 G. Loreti, A. L. Facci and S. Ubertini, *Sustainability*, 2021, **13**, 12515.